Available online at www.sciencedirect.com
SCIENCE DIRECT®
International Journal of Heat and Mass Transfer 49 (2006) 3285–3297
International Journal of HEAT and MASS TRANSFER
www.elsevier.com/locate/ijhmt

3D predictions of thermally sprayed polymer splats: Modeling particle acceleration, heating and deformation on impact with a flat substrate

Milan Ivosevic [a], Richard A. Cairncross [b,*], Richard Knight [a]

[a] Department of Materials Science and Engineering, Drexel University, PA 19104, USA
[b] Department of Chemical and Biological Engineering, Drexel University, PA 19104, USA

Received 22 July 2005; received in revised form 22 March 2006
Available online 14 June 2006

Abstract

During thermal spray deposition, jets of high temperature and high velocity gases are used to melt and accelerate materials injected into the jet and propel them toward the surface to be coated. Upon impact at the surface, multiple hot particles deform, cool and consolidate to form a coating. Mathematical models have been developed to predict the particle transport and splatting on impact with a flat substrate during the High Velocity Oxy-Fuel (HVOF) combustion spraying of polymeric materials. The predicted shapes of deformed particles exhibited good qualitative agreement with experimentally observed splats including a characteristic "fried-egg" shape with large, nearly-hemispherical, core in the center of a thin disk. These shapes were formed by polymer particles having a low temperature, high viscosity core and a high temperature, low viscosity surface.

Keywords: Thermal spraying of polymers; Solvent-free coatings; Splats; Droplet impact

1. Introduction

Thermal spray is the generic term for the family of processes in which various materials are applied to surfaces to form overlay coatings, typically to provide improved corrosion, wear or thermal protection [1,2]. The majority of thermal spray processes use thermal and kinetic energy (combustion flames, electric arcs or plasma jets) to melt and accelerate injected feedstock materials in powder, wire or rod form. The resulting molten, or nearly molten, droplets/particles are accelerated in a gas stream to velocities in the range 50 to >1000 m/s and propelled towards the surface to be coated. Upon impact at the surface they spread (splatting), consolidate and cool (solidification) to form a coating. Although thermal spraying is primarily used for the deposition of metals, ceramics and cermets, in recent years several authors have reported on the successful deposition of both thermosetting and thermoplastic polymers [3–7].

The advantages of using thermal spray processes for the deposition of polymers include: (i) solventless deposition of coatings without the use of volatile organic compounds (VOCs); (ii) the ability to coat large objects in the field (iii) the ability to apply polymer coatings with high melt viscosity; and (iv) the ability to produce "ready-to-use" coatings with limited post-deposition processing such as oven drying or curing, as is typically needed in the case of electrostatic powder coatings and solvent-based paints. Disadvantages include: (i) lower deposition efficiency, (ii) lower surface finish quality and (iii) higher process complexity, often with narrow processing windows defined by the polymer melting and degradation temperatures.

In this work, both mathematical modeling and experimental observations were correlated to better understand the transport and splat formation of Nylon-11 particles during the high velocity oxy-fuel (HVOF) combustion spray process (Fig. 1). The HVOF thermal spray process was selected due to the significantly higher gas speeds (>1000 m/s) achievable relative to other combustion driven

* Corresponding author. Tel.: +1 215 895 2230; fax: +1 215 895 5837.
E-mail address: cairncross@drexel.edu (R.A. Cairncross).

0017-9310/$ - see front matter © 2006 Elsevier Ltd. All rights reserved.
doi:10.1016/j.ijheatmasstransfer.2006.03.028

Nomenclature

a	constant in Eq. (13)
A	cross-sectional area (m^2)
b	constant in Eq. (13)
Bi	Biot number
c	constant in Eq. (13)
C_p	specific heat capacity (J/kg K)
C_D	drag coefficient
D	particle/droplet diameter (m)
D_{NZL}	nozzle exit diameter (m)
E_T	temperature dependence in Eq. (12)
$\mathbf{g}$	gravity (m/s^2)
h	heat transfer coefficient (W/m^2 K)
H_f	latent heat (J/kg)
k	thermal conductivity (W/m K)
m	mass (kg)
Ma	Mach number
n	power-low exponent in Eq. (12)
Nu	Nusselt number
Pe	Peclet number
Pr	Prandtl number
r	particle/droplet radius (m)
Re	Reynolds number
Ste	Stefan number
t	time (s)
T	temperature (K)
$\mathbf{v}$	velocity vector (m/s)
We	Weber number
x	distance (m)

Greek symbols

Γ	rate of deformation tensor
Φ	equivalence ratio
α	thermal diffusivity (m^2/s)
β	gas velocity/temperature decay constant
$\dot{\gamma}$	shear rate (s^{-1})
λ	time constant in Eq. (12) (s)
μ	dynamic viscosity (Pa s)
ρ	density (kg/m^3)

Subscripts and abbreviations

app	apparent
c	jet core length
V	velocity related
T	temperature related
g	gas
in	interface
l	liquid phase
p	particle
s	solid phase

Superscripts

o	initial value
*	maximum value

thermal spray processes. By comparison, flame spray has much lower gas speeds (<200 m/s) but has also used for the deposition of polymers. The ability to accelerate particles to higher speeds is important for the deposition of materials with high melt viscosity, including high molecular weight polymers and polymer/ceramic composites with high (>5 vol.%) ceramic reinforcement contents.

The unit process of thermal spraying is the impact of an individual droplet or particle onto a substrate to form a splat. Coating characteristics such as porosity, roughness,

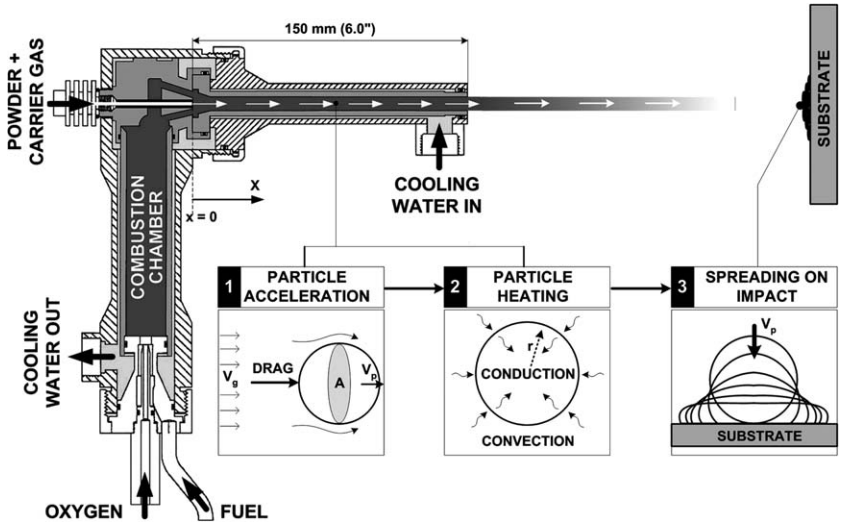

Fig. 1. Schematic of the Jet-Kote II® high velocity oxy-fuel (HVOF) thermal spray gun and three main modeling steps.

adhesive and cohesive strengths depend on the morphology of these splats and how they bond to the substrate and to each other. As a result, many studies have examined droplet impact behavior in order to better understand and improve coating processes, as summarized in the review papers of Sobolev and Guilemany [8] and Fauchais et al. [9]. Virtually all of the literature modeling splatting phenomena in thermal spray, however, have focused on metallic particles. Although in principle similar, the heating and splatting behaviors of polymer particles are fundamentally different owing to:

- The different impact flow characteristics of molten polymers compared with those of metals.
- The significantly different thermal properties and solidification kinetics.

The flow characteristics of different liquids in a given process (e.g. liquid droplets during thermal spraying) can be compared using relevant dimensionless quantities such as the Reynolds (Re) and Weber (We) numbers. The Reynolds number is the ratio of characteristic inertial to viscous flow forces, and the Weber number is the ratio of characteristic inertial to surface tension forces. The Reynolds number is typically several orders of magnitude larger for molten metals than for polymers for equally sized droplets spreading under the same conditions. For example, the isothermal splatting of molten zinc and Nylon-11 droplets of the same diameter and impact velocity results in a much thinner zinc splat of more than twice the diameter than the corresponding Nylon-11 splat [10].

Pasandideh-Fard et al. [11] showed, using a simple model of droplet spreading without solidification, that capillary effects can be neglected during droplet spreading if $We \gg Re^{1/2}$. Given that polymers typically have three to seven orders of magnitude higher melt viscosity and an order of magnitude lower surface tension than metals, the capillary effect can be neglected during molten polymer droplet spreading; i.e. the inertia is more strongly balanced by the viscous flow resistance in molten polymers and by surface tension in molten metals. The higher surface tension (lower We number) of molten metals can also lead to particle breakup into rivulets and satellites [9].

The published models of the spreading of molten metallic droplets almost exclusively assume Newtonian fluid flow described by the Navier–Stokes equations [10–15]. In molten polymers, however, this assumption would neglect the shear thinning phenomena which will be shown below to significantly affect the splat shapes. An accurate prediction of polymer splat formation during thermal spray deposition requires the polymer viscosity to be modeled as a function of both temperature and shear rate. The effect of viscoelasticity on the inertially induced spreading of polymer droplets during thermal spray processes has not yet been reported.

The thermal properties of metals and polymers differ greatly, which leads to significantly dissimilar heating characteristics of these materials. The Biot number (Bi) for a particle scales the ratio of internal and external heat transfer resistances. A low Biot number corresponds to particles heated with negligible internal resistance, resulting in a nearly uniform temperature distribution within the particle. This is typically true for most metallic and cermet materials used in thermal spraying ($Bi < 0.1$) and has led to a number of authors [13–15] neglecting temperature gradients within particles. In polymers, however, the Biot number for a particle in an HVOF jet is typically much higher ($Bi > 5$) implying that large temperature gradients will develop between the core and the surface of the particle [10]. This is consistent with the numerical analysis reported by Petrovicova [16], who predicted that HVOF sprayed Nylon-11 particles (30–60 μm in diameter) would have a steep temperature gradient developed between the surface and center of the particles. Large temperature gradients were predicted even with a rough assumption that particles are exposed to a constant gas temperature (2203 K) inside the HVOF gun nozzle and along the entire spray distance of 200 mm.

Another fundamental difference between polymer and metal splat formation processes arises from their solidification and spreading kinetics. For example, the Peclet number (Pe) for thermally sprayed polymer and metal droplets can be defined as the relative ratio of the droplets' internal heat conduction time ($t_c \sim D^2/\alpha$) and spreading time ($t_s \sim D/\mathbf{v}^o_{(p)}$) scales, where ($D$), ($\mathbf{v}^o_{(p)}$) and ($\alpha$) are the initial diameter, impact velocity and thermal diffusivity of a particle. Under typical flame spray conditions Pe for a zinc droplet is in the range 1–10 whereas Pe for a Nylon-11 droplet is almost three orders of magnitude higher ($Pe \sim 3000$) [10], indicating that the spreading and cooling of Nylon splats occur over two significantly different time scales; i.e. the effect of solidification during Nylon-11 droplet impact can be neglected. The same conclusion could be reached using the analytical model developed by Pasandideh-Fard et al. [12] which stated that solidification effects on droplet spreading could be neglected if $(Ste/Pr)^{1/2} \ll 1$. The Stefan number (Ste) is the ratio of the solidification and heat conduction time scales, and the Prandtl number (Pr) is the ratio of molecular diffusivities of momentum and heat. Although most polymers satisfy this condition, this ratio is 10.3 for a tin droplet, indicating that solidification plays a significant role in the dynamics of tin droplet spreading. The solidification that occurs during the deformation of metal droplets is one of the main causes of *jetting* and three-dimensional irregularities such as *fingering* and satellite particle *break-up* in metal splats.

The objectives of the research presented here were: (i) to improve the qualitative understanding of the acceleration and heating behavior of Nylon-11 particles during HVOF spraying using both experiments and numerical modeling, (ii) to study the effect of different particle sizes and temperature gradients developed during particle acceleration in HVOF jets on the splat formation process, (iii) to compare predicted splat shapes with experimental observations.

These objectives will help to improve the understanding of the relationships between processing conditions, splat shapes and coating microstructures of HVOF sprayed polymers.

2. Mathematical modeling

The unit operation of thermal spraying is deposition of a particle on a substrate and includes the following steps:

(i) Delivering a particle to the gun or torch.
(ii) Accelerating and heating the particle in the hot gas jet.
(iii) Splatting of the particle on impact with the substrate and in some cases.
(iv) Post-deposition flow of splats as a result of substrate preheating, heating from the jet, or a subsequent heat treatment.

Coatings are formed as a result of the deposition and consolidation of many particles, a subject that will be covered in future publications.

Mathematical modeling will be used here to predict the three key steps shown in Fig. 1: (1) particle acceleration, (2) particle heating, and (3) particle spreading on impact with a substrate. Particle acceleration and heating (steps 1 and 2 – Section 2.2) are fully coupled and were integrated simultaneously within the same FORTRAN code based on the gas flow and thermal characteristics inside the HVOF gun (Section 2.1). The particle velocity and internal temperature profile at impact were then used as the initial conditions for modeling the particle impact and deformation on a flat substrate, as described in Section 2.3.

2.1. HVOF gas flow and thermal fields

Knowledge of the combustion and exhaust gas characteristics inside the HVOF gun are essential for modeling the momentum and heat transfer to a particle (Fig. 1 – steps 1 and 2). These characteristics were determined based on calculations published by Dobbins et al. [13] using the same HVOF system (a Stellite Coatings, Inc. Jet-Kote II®) used here. The adiabatic flame temperature reported was calculated for a range of combustion chamber pressures and flame stoichiometries defined by a hydrogen-to-oxygen equivalence ratio $\Phi = (H_2/O_2)/(H_2/O_2)_{\text{stoichiometric}}$ using Chem-Sage™ thermochemical equilibrium software. At the equivalence ratio used in these experiments, $\Phi = 0.83$, the adiabatic flame temperature was ~2830 K at a combustion chamber pressure of 220 kPa (2.2 bar). Heat losses due to intensive water cooling of the HVOF gun throughout the 0.15 m (6-in.) long barrel and cylindrical combustion chamber were reported [17] to be up to 30% of the total heat input. These conditions, together with the internal gun geometry, were used to estimate a maximum jet velocity of $\mathbf{v}^*_{(g)} \sim 800$ m/s ($Mach \sim 0.6$) and temperature of $T^*_{(g)} \sim 2000$ K.

Tawfik et al. [18] proposed and experimentally verified empirical correlations for jet core length after the nozzle exit and the axial mean velocity ($\mathbf{v}_{(g)}$) of an HVOF jet with a range of validity between Mach number 0.3 and 1.4. The jet core length is a function of the nozzle exit diameter (D_{NZL}) and local Mach number (Ma), as shown in Eq. (1):

$$\frac{x_c}{D_{NZL}} = 4.2 + 1.1Ma^2 \tag{1}$$

and the axial mean velocity ($\mathbf{v}_{(g)}$) of the HVOF jet is given by

$$\mathbf{v}_{(g)} = \begin{cases} \mathbf{v}^*_{(g)}\left[1 - \exp\left(\frac{\beta_V}{1-\frac{x}{x_c}}\right)\right], & \text{for } x > x_c, \\ \mathbf{v}^*_{(g)}, & \text{for } x < x_c, \end{cases} \tag{2}$$

where ($\beta_V = 0.85$) is the gas velocity decay constant, (x) the axial distance along the gun barrel, and (x_c) the jet core length after the gun exit.

The water-cooled copper nozzle used in this work had a total length of 159.6 mm of which the entry/transition region located between the combustion head and the nozzle itself was 9.6 mm in length, the remainder (150 mm) was of constant internal diameter (6.4 mm), as shown in Fig. 1. It was assumed that adiabatic, isentropic and frictionless fluid flow conditions existed within this portion of the gun nozzle with a constant mean velocity and temperature. The mean axial gas temperature had the same functional form as the gas velocity (2) only with a larger exponential decay exponent ($\beta_T = 1.35$), as proposed by Tawfik et al. in 1997 [18]. It was also assumed that the predominant reaction product during the combustion of hydrogen and oxygen in the HVOF gun was water vapor, i.e. superheated steam. The steam properties such as density ($\rho_{(g)}$), dynamic viscosity ($\mu_{(g)}$) and thermal conductivity ($k_{(g)}$) at the gas temperature ($T = 2000$ K) were assumed to be constant and were estimated using the NIST Steam Properties Database [19].

2.2. Particle transport

The particle velocity and internal temperature profile at the moment of impact with the substrate are key inputs for determining the spreading behavior of impacting droplets. These were computed using momentum and heat transfer equations for particles in the HVOF flow field. It is commonly accepted [20] that the drag force is the dominant force governing the motion of particles in an HVOF jet, so that particle motion can be described by the following two ordinary differential equations:

$$m_{(p)}\frac{d\mathbf{v}_{(p)}}{dt} = \frac{1}{2}C_D\rho_{(g)}A_{(p)}(\mathbf{v}_{(g)} - \mathbf{v}_{(p)})|\mathbf{v}_{(g)} - \mathbf{v}_{(p)}|, \quad \mathbf{v}_{(p)}(0) = 0,$$
$$\frac{dx}{dt} = \mathbf{v}_{(p)}, \quad x(0) = 0, \tag{3}$$

where ($\mathbf{v}_{(p)}$) is the particle axial velocity, ($A_{(p)}$) the particle projection area and (C_D) the drag coefficient. The relative velocity between particles and the gas ($\mathbf{v}_{(g)} - \mathbf{v}_{(p)}$) is

multiplied by its absolute value to maintain the appropriate direction of the drag force for cases where the particle is moving faster or slower than the gas. The drag coefficient (C_D) is a function of the Reynolds number of the gas, which for the range of validity $Re_{(g)} = 0.2$–500 is in the form [21]:

$$C_D = \left(\frac{24}{Re_{(g)}}\right)\left(1 + \frac{3}{16}Re_{(g)}\right)^{\frac{1}{2}}. \tag{4}$$

This correlation was based on the assumption that the particles were spherical before impact, which is consistent with assumptions made in the heat transfer predictions and impact modeling. The Reynolds number for the relative gas flow around a particle of diameter (D) is defined as

$$Re_{(g)} = \rho_{(g)}\frac{|\mathbf{v}_{(g)} - \mathbf{v}_{(p)}|}{\mu_{(g)}}D. \tag{5}$$

As described earlier, the high Biot number of a polymer particle in an HVOF jet implies that particles are likely to develop significant temperature gradients between the core and the surface and the particle temperature should not be modeled as uniform. Accordingly, the equations describing the heat transfer from the gas to a single spherical particle (assuming spherical symmetry) with appropriate initial and boundary conditions will be as follows:

$$\begin{aligned}
&\rho_{(p)}C_{p_{(p)}}\frac{\partial T_{(p)}}{\partial t} = \frac{1}{r^2}\frac{\partial}{\partial r}\left(r^2 k_{(p)}\frac{\partial T_{(p)}}{\partial r}\right),\\
&T_{(p)}(r, t=0) = T^{o}_{(p)},\\
&\frac{dT_{(p)}}{dr}(r=0, t) = 0,\\
&-k_{(p)}\frac{dT_{(p)}}{dr}(r=R_{(p)}) = h(T_{(p)}(r=R_{(p)}) - T_{(g)}),
\end{aligned} \tag{6}$$

where ($T_{(p)}$) is the particle temperature, and ($\rho_{(p)}$), ($C_{p_{(p)}}$), and ($k_{(p)}$) are the density, heat capacity and thermal conductivity of the particle, (r) the radial distance from the center of the particle, ($R = D/2$) the particle radius and (h) the heat transfer coefficient. The heat transfer coefficient, (h), was computed by the Ranz-Marshall semi-empirical equation [22]:

$$\frac{hD}{k_{(g)}} = Nu = 2 + 0.65Re_{(g)}^{1/2}Pr_{(g)}^{1/3}, \tag{7}$$

where ($Nu = hD/k_{(g)}$) is the Nusselt number and ($Pr_{(g)} = C_{p_{(g)}}\mu_{(g)}/k_{(g)}$) the Prandtl number.

The polymer modeled was a semi-crystalline Nylon-11. The melting region, with corresponding heat of fusion, was confirmed using a Perkin Elmer model DSC-7 Differential Scanning Calorimeter (DSC). The DSC analysis of Nylon-11 indicated that melting of the crystalline fraction consumed a considerable amount of the latent heat ($\Delta H_f = 72.2$ kJ/kg). Within the mathematical model of heat transfer (Eqs. (6) and (7)) the heat consumed by melting of the polymer was accounted for by making the polymer heat capacity $C_{p_{(p)}}$ a function of temperature using the apparent heat capacity ($C_{p_{(p)}} = C_{p_{(app)}}$) method, as described by Hu and Argyropoulos [23]:

$$C_{p_{(app)}} = \begin{cases} C_{p_{(s)}} & T < T_{(s)} \quad \text{solid phase,}\\ C_{p_{(in)}} & T_{(s)} < T < T_{(l)} \quad \text{solid/liquid phase,}\\ C_{p_{(l)}} & T > T_{(l)} \quad \text{liquid phase,} \end{cases} \tag{8}$$

where

$$C_{p_{(in)}} = \frac{\left\{\int_{T_{(s)}}^{T_{(l)}} C_p(T)\,dt + \Delta H_f\right\}}{(T_{(l)} - T_{(s)})}. \tag{9}$$

The equations (Eqs. (3)–(6)) for momentum and heat transfer were solved by numerical integration using the forward Euler method with a time step small enough (10^{-7} s) that the local Reynolds number, gas velocity and temperature could be considered constant over each time step.

2.3. Particle impact and spreading

Impact and deformation of thermally sprayed droplets on a rigid surface are characterized by the complex three-dimensional large deformation of free surfaces. The splashing droplet typically is not axisymmetric, which would require a three-dimensional model for realistic splat predictions. Arbitrary Lagrangian–Eularian (ALE) based finite element methods, such as the one published by Cairncross et al. in 1999 [24] using a moving boundary-fitted mesh, were proven to successfully track large deformations and rotations of free surface boundaries in three-dimensional fluid flows. Although this approach can be very accurate with respect to small scale viscous free surface flows, the droplet splashing including the creation of new surfaces during fingering and/or generation of satellites and breakups are not amenable to boundary-fitted techniques. Three dimensional, highly irregular, free surface flows including creation of new surfaces have been commonly solved using fixed-grid Eulerian-boundary tracking methods (e.g. volume of fluid methods (VoF) [25]) such as that used here, Flow-3D® (version 9.0). This VoF method uses a fixed-grid volume tracking algorithm to track the fluid deformation and droplet free surface based on the fluid fraction function defined to be equal to unity in the fluid and zero outside the fluid. The computational domain including fixed grid and a schematic representation of the initial and boundary conditions used here is shown in Fig. 2. Flow-3D® was used to predict splat shapes using results from the acceleration and heating models as initial conditions. The predicted particle temperature profiles at impact were included in Flow-3D® through a user-defined subroutine using a sixth order polynomial representation.

Trapaga and Szekely [26] used an earlier version of the Flow-3D® software to model the isothermal spreading of a metallic droplet under conditions typical for thermal spraying, assuming Newtonian fluid flow with a constant contact angle. The splashing of a molten metal droplet, however, requires heat transfer and solidification models to be

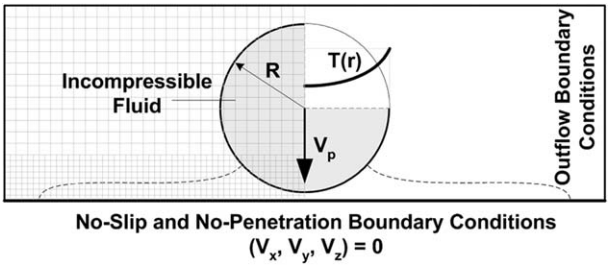

Fig. 2. Boundary conditions, initial conditions and cross-section of a typical mesh used in Flow-3D®.

included because solidification and spreading occur over similar time scales [27]. In this model, solidification, heat transfer from the splat to the substrate and capillary effects, which were all proven [10] to have secondary effects on the spreading of a molten polymer droplet, were neglected. Conductive and convective heat transfer inside the splat were computed using a heat transfer equation as follows:

$$\rho_{(\mathrm{p})} C_{p_{(\mathrm{p})}} \left(\frac{\partial T_{(\mathrm{p})}}{\partial t} + \mathbf{v} \cdot \nabla T_{(\mathrm{p})} \right) = k_{(\mathrm{p})} \nabla^2 T_{(\mathrm{p})}, \tag{10}$$

where ($\mathbf{v}$) is the local fluid velocity inside a deforming droplet. Fluid flow of a spreading polymer droplet was modeled as generalized Newtonian flow using a momentum Eq. (11) in a 3D Cartesian coordinate system:

$$\rho_{(\mathrm{p})} \left(\frac{\partial \mathbf{v}}{\partial t} + \mathbf{v} \cdot \nabla \mathbf{v} \right) = \rho_{(\mathrm{p})} \mathbf{g} - \nabla p + \nabla \cdot \left[\mu(\Gamma, T_{(\mathrm{p})}) (\nabla \mathbf{v} + \nabla \mathbf{v}^{\mathrm{T}}) \right]. \tag{11}$$

A generalized Newtonian fluid differs from a Newtonian fluid in that viscous stress is a nonlinear function of the rate of separation ($\boldsymbol{\Gamma} = 0.5(\nabla \mathbf{v} + \nabla \mathbf{v}^{\mathrm{T}})$). In other words the dynamic viscosity (μ) in Eq. (11) is a function of the rate of the deformation tensor ($\boldsymbol{\Gamma}$). A scalar measure of the rate of strain, or shear rate, is $\dot{\gamma} = 2\Gamma \equiv (\Gamma : \Gamma)^{1/2}$. In this paper the viscosity includes both shear thinning and temperature dependence ($\mu(\dot{\gamma}, T)$) using the Carreau model [28] of the form:

$$\mu = \mu_\infty + \frac{\mu_0 E_{\mathrm{T}} - \mu_\infty}{\left[1 + (\lambda E_{\mathrm{T}})^2 \dot{\gamma}^2 \right]^{\frac{1-n}{2}}}, \tag{12}$$

where the temperature component is given by

$$E_{\mathrm{T}} = \exp\left[a \left(\frac{T^*}{T - b} - c \right) \right], \tag{13}$$

where ($\mu_\infty = 0$) and ($\mu_0 = 1300$ Pa s at $T^* = 240$ °C) are the infinite and zero shear-rate viscosities, respectively, ($\lambda = 1$ s) a time constant, ($n = 0.7$) the "power-low exponent" and ($a = 16$), ($b = 0$) and ($c = 1$) constants for the temperature dependence. All curve-fitting coefficients in the Carreau model were determined based on experimental viscosity data. The viscosity of molten Nylon-11 was measured using a Rheometrics model 6 viscometer using the cone and plate method. The measurements were conducted for shear rates ranging from 0.0001 to 1.0 s^{-1} at 200, 220 and 240 °C (Fig. 3a). The data were combined with the viscosity measurements from a capillary viscometer, provided

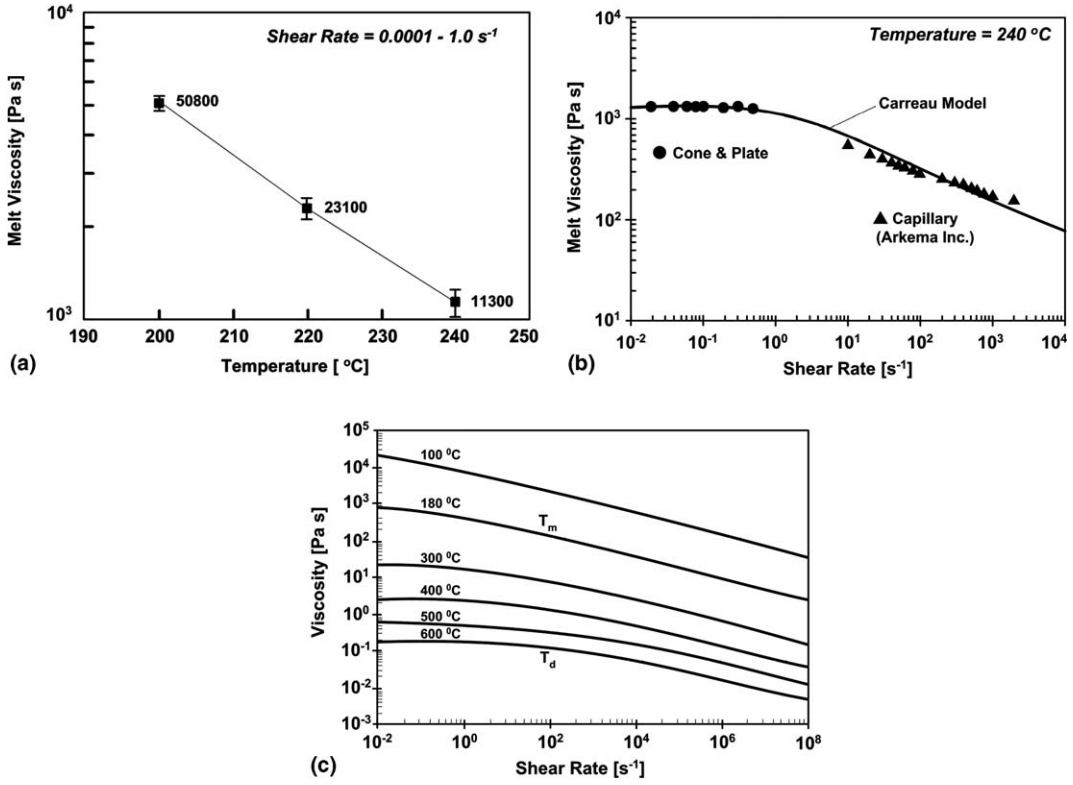

Fig. 3. Polymer viscosity data: (a) temperature-dependent zero shear rate melt viscosity and (b) melt viscosity of Nylon-11 as a function of shear rate at 240 °C. (c) Shear rate and temperature-dependent viscosity of Nylon-11 predicted using a Carreau model (Eqs. (12) and (13)).

by powder manufacturer (Arkema, Inc.), for a viscosity-to-shear rate dependence up to $10^4\ s^{-1}$ (Fig. 3b). The shear rate and temperature-dependent viscosity model of Nylon-11, predicted using the Carreau model (Eqs. (12) and (13)) based on the experimental measurements, is shown in Fig. 3c.

In order to better understand the nature of inertially induced viscous droplet deformation and the importance of the shear thinning phenomena, several base-case comparisons were conducted for Newtonian and shear thinning droplets. The three-dimensional spreading progression at characteristic dimensionless times ($t^* = t/(D/\mathbf{v}^{o}_{(p)})$) were generated for 60, 90 and 120 μm diameter particles. These particle sizes were chosen to cover the particle size range of polymeric powders typically used for thermal spraying and in the experiments described in the following section.

3. Experimental evaluations

Semi-crystalline Polyamide-11 (Nylon-11) powders, commercially available as Rilsan PA-11 French Natural ES D-60 and D-120 (donated by Arkema, Inc.) were used as the feedstock for the thermal spray experiments reported. The as-received powders had a nominal mean particle size of 60 and 120 μm. The melting and degradation temperatures of Nylon-11, as reported by the manufacturer, were in the range 182–191 °C and 357–557 °C, respectively.

Swipe or "splat" tests comprising single high speed (>0.7 m/s) passes of the spray gun across *room temperature* glass slides were conducted at low powder feed rates ($\sim 3\times10^{-5}$ kg/s) to observe the morphology of individual splats. Nylon-11 particles were also deposited onto a substrate preheated to ~190 °C in order to better understand the influence of substrate preheating on the deposition behavior of the Nylon-11 material. Splat tests were carried out using a Stellite Coatings, Inc. Jet-Kote II® HVOF spray system (Fig. 1) using oxygen and hydrogen flow rates of 0.0024/0.0039 m^3/s (300/500 scfh), respectively, and a spray distance of 225 mm. The spray nozzle used was 150 mm long with an internal diameter of 6.4 mm. The same equipment and spray parameters were also used to deposit a ~400 μm thick D-60 and D-120 Nylon-11 coatings onto grit blasted 1018 steel substrates. The resulting coatings were prepared using standard metallographic techniques: sectioning, mounting and polishing. The coating cross-section and splat morphologies were analyzed by optical microscopy (Olympus PMG-3 optical metallograph).

In-flight particle velocities at a distance of 100 mm from the HVOF gun nozzle exit were measured using a *SprayWatch 2i* (Oseir Ltd, Tampere, Finland) system in conjunction with a diode laser illumination source. Measurements were conducted at oxygen and hydrogen gas flow rates of 0.0024 and 0.0039 m^3/s, (300 and 500 scfh) respectively (a total gas flow rate of 1.86×10^{-3} kg/s at $\Phi = 0.83$), the same parameters used for coatings and splat deposition. A total of 306 individual particles were recorded.

One of the important characteristics of thermal spraying in general is that a relatively large number of process parameters need to be controlled during the spray process. Although this is often challenging with respect to process repeatability, it also increases the number of parameter combinations that can be varied in order to achieve specific coating microstructures. The HVOF spray parameters used during these experiments were chosen as a baseline case to be used as a reference for the numerical model development.

4. Results and discussion

The results of the three modeling steps described above, including particle acceleration and heating in an HVOF jet and particle spreading on impact with a substrate, are presented in Sections 4.2, 4.3 and 4.4. For all simulations, except where stated otherwise, the parameters listed in Table 1 were used. The experimental observations used to support and evaluate the accuracy of the numerical models are summarized in the following section.

4.1. Experimental observations

Numerous spray trials were conducted to determine the process parameters that reliably produced adherent Nylon-11 coatings, as shown in Fig. 4a and b. These spray parameters were by no means fully optimized or the only HVOF spray parameters that could produce similar Nylon-11 coatings. A numerical model developed around the experimental base-case parameters, however, can be used for further process optimization for increased deposition efficiency and lower porosity and particle degradation, *via* parametric studies. The cross-sectional images of Nylon-11 coatings, deposited using two different nominal particle sizes: D-60 (Fig. 4a) and D-120 (Fig. 4b) under the same spray conditions, indicated that unmelted or partially melted larger particles (i.e. 120 μm) did not deform readily, leading to a porous coating (Fig. 4b).

A critical link for better understanding the relationship between the HVOF process parameters and coating microstructure is the individual splat formation process as the unit step. The morphologies of Nylon-11 splats deposited during a swipe test onto room temperature and preheated

Table 1
Parameters used in mathematical modeling

Nylon-11 Particle	HVOF Gas (superheated steam @ 2000 K)
$\rho_{(p)} = 1030$ kg/m^3	$\rho_{(g)} = 150$ kg/m^3
$k_{(p)} = 0.19$ W/mK	$k_{(g)} = 0.20$ W/mK
$\Delta H_f = 72.2$ kJ/g	$\mu_{(g)} = 7\times10^{-5}$ Pa s
$C_{p_{(p)}}$ [a] $= 1753$ J/kg K	$C_{p_{(g)}} = 5000$ J/kg K

[a] Heat capacity of the Nylon-11 at room temperature.

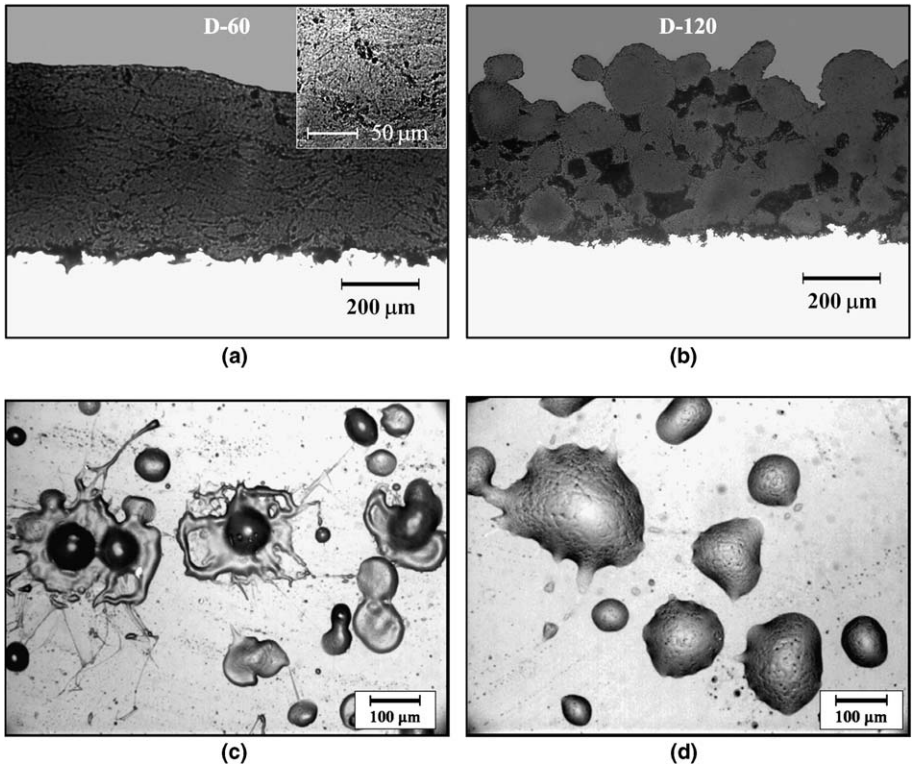

Fig. 4. Cross-sections of HVOF sprayed Nylon-11 coatings on grit-blasted 1018 steel substrates (average roughness $Ra = 2.96$ μm) (a) D-60 and (b) D-120 powders used. Nylon-11 splats deposited *via* swipe tests onto a glass slide (c) substrate at room temperature, (d) substrate preheated to ~190 °C.

glass slides are shown in Fig. 4c and d. When the substrate was at room temperature, most of the larger splats (>100 μm) exhibited a characteristic "fried-egg" shape with a large, nearly-hemispherical, core in the center of a thin disk (Fig. 4c). This shape indicated the existence of a large radial difference in the flow properties of the molten surface of the Nylon-11 droplets and the largely unmelted core; i.e. the "fried-egg" shaped splats were formed by polymer particles having a large radial temperature profile – a low temperature, high viscosity core and a high temperature, low viscosity surface.

When the substrate was preheated, the splats exhibited a flattened hemispherical shape (Fig. 4d). This was attributed to post-deposition flow activated by surface tension, viscoelastic effects and/or residual stress after the initial "fried-egg" splats were fully melted by the preheated substrate. Other experiments confirmed that post-deposition flow of Nylon-11 splats occurred only when the substrate was preheated to ~170 °C or above, which corresponded to the Nylon-11 melting region. This indicated that the morphology of the initially sprayed particles could be changed using substrates preheated to temperatures near the melting point of the polymer being sprayed, as reported by Brogan and Berndt [4]. The morphology and wetting of the initial splats on the substrate surface are critical for the overall integrity of the coating/substrate interface. Detailed experiments and modeling of post-deposition flow of a thermally sprayed Nylon-11 droplet on a preheated substrate is in progress and will be reported separately.

4.2. Particle velocity

The acceleration of particles in the HVOF jet was predicted by solving Eqs. (3)–(5), and results are shown in Fig. 5. The predicted velocities of 30, 60, 90 and 120 μm diameter particles at the moment of impact on the substrate at a spray distance of 225 mm were 537, 497, 427 and 368 m/s. In general, polymer particles accelerate in HVOF jets much faster than similarly sized metallic or cermet particles [18,20]. This is due to the much lower density

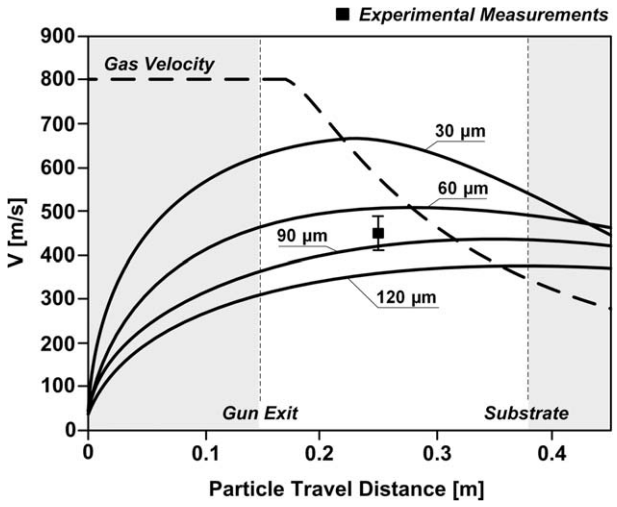

Fig. 5. Predicted particle and gas velocities combined with experimental measurements at a spray distance of 100 mm from the gun exit.

of polymers (900–1400 kg/m^3) versus that of metals or cermets (~2700–15,000 kg/m^3). Similarly, polymer particles have lower inertia and their velocity responds more rapidly to the decreasing gas velocity after exiting the gun nozzle. One way to increase the impact velocity, and therefore the kinetic energy of polymer particles, would be to minimize the spray distance. This approach, however, has limited use due to the potentially destructive effect of the jet on the polymeric coating at low gun surface speeds (<0.1 m/s) [29].

A much higher particle velocity was predicted by Petrovicova [16] (up to 1480 m/s for a 30 μm diameter Nylon-11 particle), however, Petrovicova modeled a supersonic HVOF gas flow ($Ma = 1.5$–2.4) assuming that the axial gas velocity was constant along the entire spray distance. The base-case HVOF parameters used here and modeled included subsonic gas velocity ($Ma = 0.6$) with no shock diamonds and a non-constant axial gas velocity profile (Fig. 5).

The results of the in-flight particle velocity measurements carried out using the *SprayWatch 2i* system were combined with the numerical velocity predictions in Fig. 5. The mean particle velocity 100 mm downstream of the gun exit was 433 m/s with a standard deviation of 20 m/s, based on a count of 306 particles. The measured particle velocities compared well with the predicted velocities for 60–90 μm diameter particles. This was expected since this particle size range covers ~70% of the total Nylon-11 feedstock volume used during the experimental measurements.

4.3. Particle heating

The heat transfer from the combusting gas to the Nylon-11 particles was predicted by solving Eqs. (6) and (9) simultaneously with the momentum transfer Eqs. (3)–(5) for particle acceleration in the HVOF jet. The results for a single 90 μm particle are shown in Fig. 6a, while the temperature profiles within 30, 60, 90 and 120 μm diameter particles immediately before impact with a substrate are shown in Fig. 6b.

Forced convection from the HVOF jet to a micron-sized particle is characterized by a high convective heat transfer coefficient ($h \sim 5000$–$17{,}000$ W/(m^2 K)). This results in a rapid increase in particle surface temperature, which for a 90 μm diameter particle reaches almost half of the gas temperature (~900 °C) within the first third of the nozzle length (Fig. 6a). Similarly, the particle surface temperature cooled slightly following the decrease in jet temperature after exiting the gun, as shown in the same figure. Despite the rapid rise in particle surface temperature, the high internal thermal resistance (high *Bi* number) of Nylon-11 particles prevents the interior of the particle from being heated at the same rate. As a result, a 90 μm diameter particle develops a steep temperature gradient between its core and surface. The core region (<36 μm: $r/R = 0.4$) is below the melting temperature of Nylon-11 (182–191 °C) while the surface region (>77 μm: $r/R = 0.85$) has a temperature exceeding the upper degradation limit of the polymer (560 °C). Similarly, a 120 μm diameter particle was predicted to have an unmelted core and surface temperature above the degradation temperature, whereas a 60 μm diameter particle was predicted to be fully melted, but with almost 50% of its volume above the degradation temperature. The surface temperature of a 30 μm diameter particle under the HVOF conditions used was more than twice as high as the upper degradation limit, indicating that such small particles will most likely be fully degraded during spraying. Theoretically, a 30 μm particle even develops an inverted temperature profile with a higher temperature in the core than at the surface (Fig. 6b).

According to the numerical predictions, particles smaller than ~40 μm in diameter and the surfaces of larger particles exceed the degradation temperature of Nylon-11 under the spray conditions used. The particles, however, have a very short residence time under these conditions (~0.7–1.5 ms). A better understanding of potential polymer degradation during HVOF spraying and more accurate mathematical predictions requires a consideration of the polymer degradation kinetics. This topic is beyond the scope of this paper and it will be treated as a separate subject. In the following section, the predicted temperature

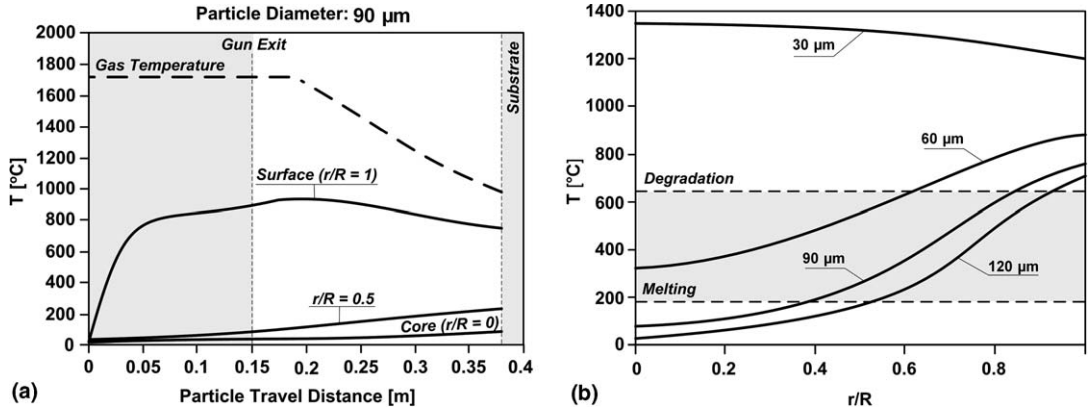

Fig. 6. (a) Temperature of a 90 μm diameter particle with respect to travel distance. (b) Particle temperature profile within Nylon-11 particles immediately before impact with a substrate at 225 mm spray distance.

profiles within the particles will be used as the initial conditions for the impact and deformation model, as presented in Fig. 6b, assuming that no degradation occurred.

4.4. Particle deformation

The Reynolds number of a deforming droplet scales the viscous dissipation of the inertial forces for inertially induced deformation (see Eq. (14)). When surface tension and solidification are negligible, the Reynolds number is the key dimensionless quantity governing the flow behavior:

$$Re = \frac{\text{Inertia}}{\text{Viscous Dissipation}} = \frac{\rho_{(p)} \mathbf{v}_D}{\mu_{(p)}}. \quad (14)$$

Dynamic flow conditions at the moment of particle impact are also commonly compared using an *impact Reynolds number* ($Re^o = (\rho_{(p)} \mathbf{v}^o_{(p)} D)/\mu_{(p)}$) defined by the droplet density ($\rho_{(p)}$), original diameter (D), impact velocity ($\mathbf{v}^o_{(p)}$) and dynamic viscosity ($\mu_{(p)}$). After the first moment of particle impact, the parameters in Re^o will change rapidly such that a new *local Reynolds number* (Re) can be defined at every moment and position during fluid flow until the droplet is fully spread. If the Re^o is high and approximately uniform across the droplet, inertia forces dominate, resulting in a large degree of deformation (Fig. 7a-IV) as usually seen during the spreading of a Newtonian fluid droplet with uniform internal temperature distribution. Conversely, if Re^o is low, and particularly if it is less than 1 across the entire droplet, viscosity forces dominate over inertia and the result is a low degree of droplet deformation (Fig. 7a-I). A low impact Reynolds number ($Re^o < 1$) is rare in engineering practice, especially in the context of common coating and droplet consolidation processes such as liquid spray painting and inkjet printing or even thermal spraying of metals. This is because the viscosity of these liquid droplets is significantly lower than that of molten polymer droplets and because the low Re number flow conditions do not generate sufficient degree of droplet deformation as required by those coating processes.

The viscosity of thermally sprayed polymer particles is usually non-uniform across an impacting droplet. It is different at the surface and center of the droplet, which can be due to: (i) differences in shear rate, (ii) differences in temperature and (iii) differences in composition (i.e. hollow or composite particles). Differences in viscosity lead to different characteristic Re for the surface and center of the droplet. For example, a molten polymer droplet, with strong shear thinning behavior and lower core temperature, has a non-uniform Re^o number – higher at the particle surface and lower at the core. These flow conditions are likely to generate "fried-egg" shaped splats with an elevated core in the center of a thin disk, as shown in Fig. 7a-II. The opposite case, where the Re^o is lower at the particle surface than at the core (Fig. 7a-III) is a special case which can occur during the impact of hollow or composite particles with significantly lower viscosity in the particle core than at the surface.

The thermal spraying of polymer powders is unique because impacting particles can have a broad range of impact Reynolds numbers ($Re^o = 10^{-3}$–10^6), depending on the degree of in-flight melting. For example, the zero shear rate viscosity of Nylon-11 at 200 °C is ~5000 Pa s (Fig. 3a). Under the base-case HVOF conditions used here, the impact Reynolds number of a 90 μm diameter droplet with this viscosity would be on the order of $\sim 10^{-2}$, resulting in only slight deformation of the droplet (Fig. 7a-I). The viscosity of a deforming polymer droplet at constant

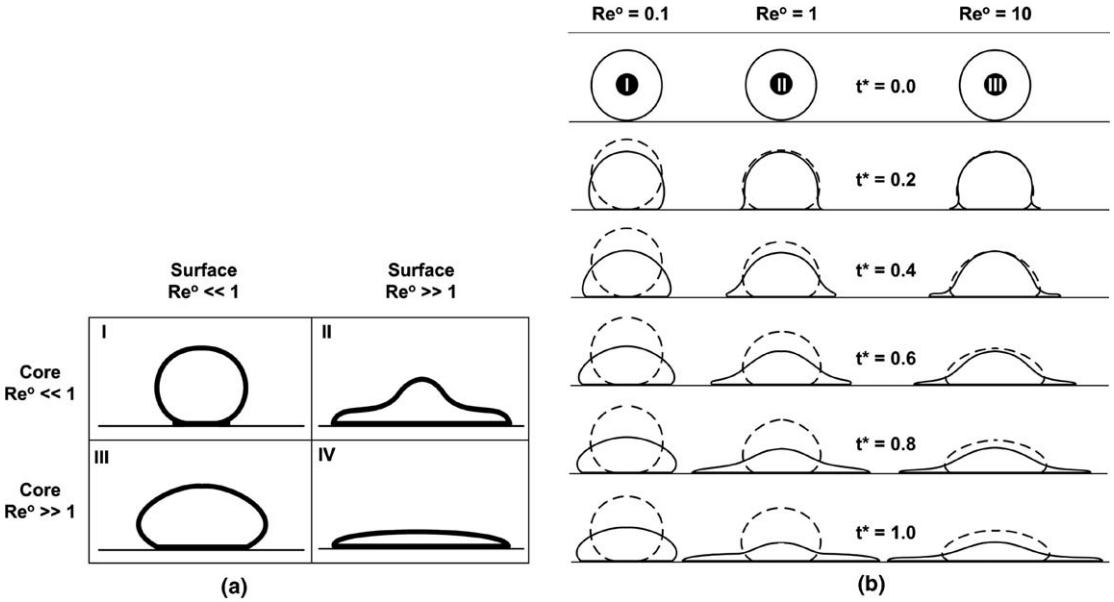

Fig. 7. (a) Sketches of characteristic splat profiles as a result of different Re^o numbers at particle surface and core. (b) Predicted splat cross-sections during the isothermal spreading of a Newtonian (dashed line) and a shear thinning fluid (solid line).

temperature also varies due to shear thinning, where the viscosity decreases as the shear rate increases (Fig. 3b and Eq. (12)). While the temperature effect on viscosity is relatively easy to comprehend, the magnitude and importance of shear thinning on polymer droplet deformation is often not so obvious. The shear thinning effect on isothermal spreading of a polymer droplet is illustrated in Fig. 7b.

Newtonian (Fig. 7b-dashed line) and shear thinning (Fig. 7b-solid line) droplet deformations were predicted under the same impact conditions ($\mathbf{v}^{o}_{(p)}, D, \rho_{(p)}$). Three characteristic cases were compared, including impact Reynolds number of the Newtonian fluid droplet equal to 0.1, 1 and 10, and shear thinning droplets with the low shear rate viscosity (up to $\sim 1\ s^{-1}$, Fig. 3b) equal to the viscosity of the corresponding Newtonian fluid droplet. The shear thinning droplet effect (Fig. 7b-solid line) was predicted using the Carreau model (Eq. (12)) without temperature dependence ($E_T = 1$) and an impact shear rate of $D/\mathbf{v}^{o}_{(p)} \sim 10^6\ s^{-1}$ which was typical of HVOF spraying. The model also included a shear thinning exponent $n = 0.7$, based on experimental viscosity measurements (Fig. 3b). Under these conditions, the surface viscosity of a shear thinning droplet was in the range $\sim$10–50 Pa s and corresponding impact Reynolds number on the order of $\sim 10^4$.

When the impact Reynolds number is less or equal to 1 (Fig. 7b-I, II), isothermal spreading of a Newtonian fluid droplet results in very small deformation, similar to the sketch shown in Fig. 7a-I. Under the same impact conditions, shear thinning reduces the viscosity at the beginning of droplet deformation, when the shear rate is the largest, sufficiently that the droplet experiences a significantly higher degree of deformation than the corresponding Newtonian droplet (Fig. 7b). The shear thinning droplets also have a tendency to spread into thin disks with small elevation in the center (Fig. 7b-II, III) due to the lower shear rate and higher viscosity at the droplet core. The comparison between the spreading of shear thinning versus Newtonian fluid droplets under HVOF spraying conditions indicated a major effect of shear thinning on the flow dynamics of a spreading droplet. The magnitude of this effect is predominantly governed by the extremely high impact shear rate ($\mathbf{v}^{o}_{(p)}/D \sim 10^6\ s^{-1}$) of the HVOF sprayed particles.

Most of the polymer particles under HVOF conditions have higher temperatures at the surface than at the core (Section 4.3). Accordingly, the local Reynolds number varies across the droplet due to the temperature-dependent viscosity distribution. Particles with a radial temperature profile i.e. a low temperature, high viscosity core and a high temperature, low viscosity surface, will deform into "fried-egg" shaped splats, as shown in Fig. 7a-II. When the particle starts deforming, the particle viscosity is also altered based on the local fluid velocity. The shear rate and temperature-dependent viscosity of Nylon-11 (Fig. 3c), predicted using the Carreau model (Eqs. (12) and (13)), is used for three-dimensional splat predictions. In this model solidification of the droplet was modeled only through a temperature-dependent viscosity. The portion of the droplet below the melting temperature (<182 °C) was still considered liquid, however, with a viscosity sufficiently high (>10^3 Pa s) (Fig. 3c) so that it would not deform significantly on impact. This viscosity was just a natural extension of the temperature-dependent viscosity in Fig. 3a into a low temperature region.

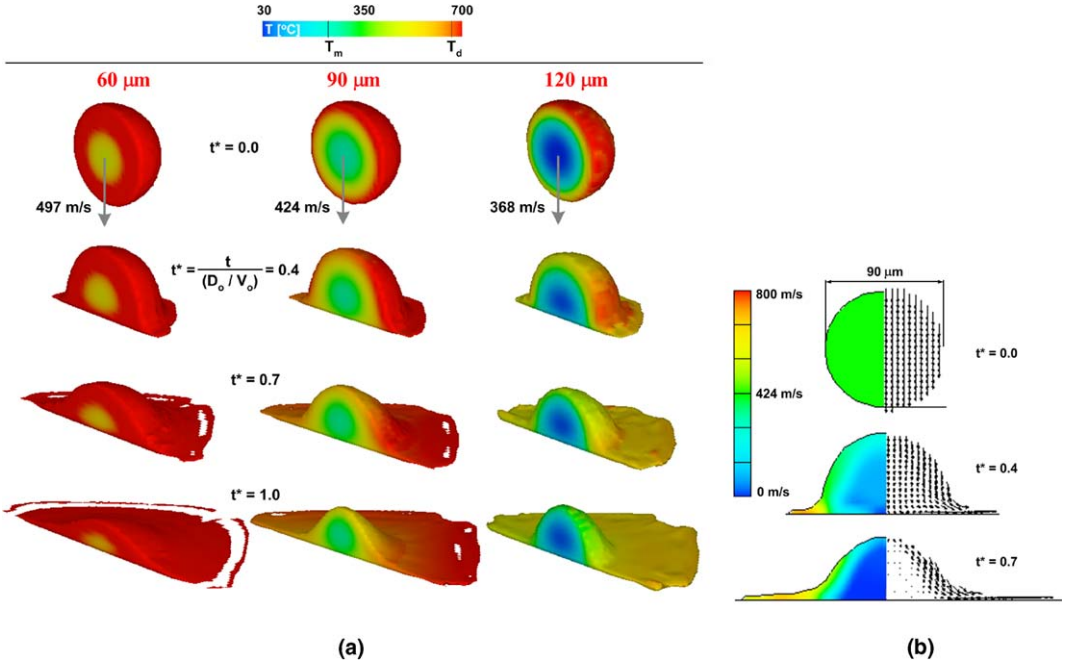

Fig. 8. (a) Cross-sections of predicted three-dimensional spreading splats for 60, 90 and 120 μm diameter particles. (b) Velocity field inside a spreading 90 μm diameter particle; left-hand side: velocity magnitude, right-hand side: velocity vectors.

Particle impact velocity (Fig. 5), temperature profile with neglected polymer degradation (Fig. 6b) and temperature and shear rate dependent viscosity (Fig. 3c) were all combined together as a part of three-dimensional deformation model, the results of which are summarized in Fig. 8. The predicted splat shapes shown in Fig. 8a exhibited a good qualitative agreement with the experimentally observed splat shapes shown in Fig. 4c. The larger, 90 and 120 μm diameter particles were spread into "fried-egg" splats with large nearly-hemispherical cores in the centers of thin disks, whereas 60 μm diameter particle generated flattened splats with small elevations in the center. This was consistent with the predicted internal temperature profiles, since both the 90 and 120 μm diameter particles had unmelted cores, as shown earlier in Fig. 6b. In addition, a larger unmelted portion of the 120 μm diameter particle transformed into a larger central "dome" than for a splat arising from a 90 μm diameter particle. The 60 μm diameter particle generated rim with breakup and satellites radiating from the splat edge. This was expected since the smaller particles had higher temperatures and lower viscosities around their surfaces.

The velocity field inside a 90 μm diameter particle during spreading on impact with a flat substrate is shown in Fig. 8b. The velocity field vectors shown in the right-hand side of the droplet indicates that the characteristic "fried-egg" splat shape was formed as a low viscosity "skin" flowed around a high viscosity core. The velocity magnitude shown in the left-hand side of the droplet (Fig. 8b) indicated that after impact the droplet developed a *leading rim* with relative velocity almost double the original impact velocity ($\mathbf{v}^{o}_{(p)}$). The high velocity at the rim was the result of the squeezing flow between the fairly rigid particle core and the rigid substrate. A combination of this high velocity and the no-slip boundary condition at the substrate surface generates shear rates almost three orders of magnitude higher ($\sim 10^9\ s^{-1}$) than the characteristic shear rates ($\mathbf{v}^{o}_{(p)}/D \sim 10^6\ s^{-1}$) at impact. Very high shear rates lead to low viscosity due to shear thinning resulting in the very thin rim (2–5 μm) of the splat. The low viscosity in the rim also contributes toward the formation of break-ups and satellites, as predicted in Fig. 8a for 60 μm diameter particle.

5. Conclusions

One of the principal goals of this work was to develop a knowledge base and improved qualitative understanding of the transport and impact behavior of polymeric particles during the HVOF combustion spray process. Mathematical models of (1) the acceleration, (2) the heating and (3) the deformation of Nylon-11 particles have been developed. Heating and acceleration were fully coupled and calculated within the same FORTRAN code. Results from the particle heating and acceleration computations were used as the initial conditions for modeling the particle deformation on impact with a substrate using the Flow-3D® computational fluid dynamic software.

Molten Nylon-11 was modeled as a generalized Newtonian fluid with temperature and shear rate dependent viscosity. Shear thinning was demonstrated to have a major effect on the flow dynamics of a spreading droplet because it significantly reduces the viscosity at the beginning of droplet deformation when the shear rate is the highest. Shear thinning causes an increase in the droplet spreading ratio and generates splats with significantly higher degrees of deformation than Newtonian droplets under the same impact conditions (i.e. impact Reynolds number). While shear thinning primarily affects droplet spreading ratio, the internal temperature distribution has the largest effect on the final splat shape, particularly when particles are partially melted. The predictions showed that larger (i.e. 90–120 μm diameter) polymer particles developed steep internal temperature gradients between the core and the surface during HVOF spraying. The prediction was in agreement with experimental observations of thermally sprayed splats, since most large Nylon-11 splats sprayed onto a room temperature substrate exhibited a characteristic "fried-egg" shape. This shape was formed by polymer particles having a low temperature, high viscosity core and a high temperature, low viscosity surface.

Theoretical predictions and experiments presented indicate that the HVOF combustion spray process is a viable method for the solvent-free deposition of polymers. The models also pointed out several potential process drawbacks, such as the possibility of overheating small (i.e. $<$40 μm) particles and incomplete melting of larger ones (i.e. $>$70 μm). Addressing these issues may not only help to improve the understanding of the relationships between processing conditions, splat morphology and coating microstructure of HVOF sprayed polymer coatings but also help with the development of a new low temperature thermal spray process. An optimal thermal spray process for polymers should use a low gas temperature (~100–500 °C) to prevent overheating of the polymer particles, a high gas velocity to provide high kinetic energy for spreading of the high melt viscosity particles and a sufficiently long dwell time for uniform particle melting.

Acknowledgements

The authors would like to acknowledge the financial support by the National Science Foundation (NSF DMI-0209319). The views expressed in this paper do not necessarily reflect those of NSF. The authors would also like to thank Arkema Corporation for donating the Nylon-11 powders and Oseir Ltd. for help during particle velocity measurements. The authors greatly appreciate the assistance and help of Mr. Dustin Doss and Dr. Thomas E. Twardowski. The authors also acknowledge the help of undergraduate student Ms. Shannon Lafferty during Nylon-11 viscosity measurements.

References

[1] J.R. Davis et al. (Eds.), first ed., Handbook of Thermal Spray Technology, ASM International®, Materials Park, OH, 2004.

[2] P. Fauchais, A. Vardelle, B. Dussous, Quo vadis thermal spraying? J. Thermal Spray Technol. 10 (1) (2005) 44–66.

[3] T. Zhang, D.T. Gawne, Y. Bao, The influence of process parameters on the degradation of thermally sprayed polymer coatings, Surf. Coat. Technol. 96 (1997) 337–344.

[4] J.A. Brogan, C.C. Berndt, The coalescence of combustion-sprayed ethylene-methacrylic acid copolymer, J. Mater. Sci. 32 (1997) 2099–2106.

[5] E. Petrovicova, R. Knight, L.S. Schadler, T.E. Twardowski, Nylon-11/silica nanocomposite coatings applied by the HVOF process: I. Microstructure and morphology, J. Appl. Polym. Sci. 77 (8) (2000) 1684–1699.

[6] E. Petrovicova, L.S. Schadler, Thermal spray of polymers, Int. Mater. Rev. 47 (4) (2002) 169–190.

[7] M. Ivosevic, R. Knight, S.R. Kalidindi, G.R. Palmese, J.K. Sutter, Adhesive/cohesive properties of thermally sprayed functionally graded coatings for polymer matrix composites, J. Thermal Spray Technol. 14 (1) (2005) 45–51.

[8] V.V. Sobolev, J.M. Guilemany, Flattening of droplets and formation of splats in thermal spraying: a review of recent work – Part 1, J. Thermal Spray Technol. 8 (1) (1999) 87–101.

[9] P. Fauchais, M. Fukomoto, A. Vardelle, M. Vardelle, Knowledge Concerning Splat Formation: An Invited Review, J. Thermal Spray Technol. 13 (3) (2004) 337–360.

[10] M. Ivosevic, R.A. Cairncross, R. Knight, Heating and impact modeling of HVOF sprayed polymer particles, in: Proceedings of the 2004 International Thermal Spray Conference (ITSC-2004), DVS/IIW/ASM-TSS, Osaka, Japan, 2004.

[11] M. Pasandideh-Fard, Y.M. Qiao, S. Chandra, J. Mostaghimi, Capillary effects during droplet impact on a solid surface, Phys. Fluids 8 (3) (1996) 650–659.

[12] M. Pasandideh-Fard, R. Bhola, S. Chandra, J. Mostaghimi, Deposition of tin droplets on a steel plate: simulations and experiments, Int. J. Heat Mass Transfer 41 (1998) 2929–2945.

[13] T.A. Dobbins, R. Knight, M.J. Mayo, HVOF thermal spray deposited Y_2O_3-stabilized ZrO_2 coatings for thermal barrier applications, J. Thermal Spray Technol. 12 (2) (2003) 214–225.

[14] M. Pasandideh-Fard, V. Parshin, S. Chandra, J. Mostaghimi, Splat shapes in a thermal spray coating process: simulations and experiments, J. Thermal Spray Technol. 11 (2) (2002) 206–217.

[15] M. Li, P.D. Christofides, Feedback control of HVOF thermal spray process accounting for powder size distribution, J. Thermal Spray Technol. 13 (1) (2004) 108–120.

[16] E. Petrovicova, Structure and properties of polymer nanocomposite coatings applied by the HVOF process, Ph.D. Dissertation, Drexel University, 1999.

[17] M.L. Thorpe, H.J. Richter, A pragmatic analysis and comparison of HVOF processes, J. Thermal Spray Technol. 1 (2) (1992) 161–170.

[18] H.H. Tawfik, F. Zimmerman, Mathematical modeling of the gas and powder flow in HVOF systems, J. Thermal Spray Technol. 6 (3) (1997) 345–352.

[19] NIST/ASME Steam Properties Database Software, Version 2.21, NIST, Gaithersburg, MD, 1995.

[20] D. Cheng, G. Trapaga, J.W. McKelling, E.J. Lavernia, Mathematical modeling of high velocity oxygen fuel thermal spraying: an overview, Key Eng. Mater. 197 (2001) 1–26.

[21] J.F. Douglas, J.M. Gasiovek, J.A. Swaffield, Fluid Mechanics, third ed., Longman Group Limited, 1995.

[22] R.B. Bird, W.E. Stewart, E.N. Lightfoot, Transport Phenomena, Wiley, New York, USA, 1960.

[23] H. Hu, S.A. Argyropoulos, Mathematical modeling of solidification and melting: a review, Model. Simul. Mater. Sci. Eng. 4 (4) (1996) 371–396.

[24] R.A. Cairncross, P.R. Schunk, T.A. Baer, R.R. Rao, P.A. Sackinger, A finite element method for free surface flows of incompressible fluids in three dimensions: Part I. Boundary fitted mesh motion, Int. J. Numer. Meth. Fluids 33 (2000) 375–403.

[25] C.W. Hirt, B.D. Nichols, Volume of fluid (VoF) method for the dynamics of free boundaries, J. Comput. Phys. 39 (1981) 201–225.

[26] G. Trapaga, J. Szekely, Mathematical modeling of the isothermal impingement of liquid droplets in spraying processes, Metall. Trans. B 22 (1991) 901–912.

[27] M. Pasandideh-Fard, S. Chandra, J. Mostaghimi, A three-dimensional model of droplet impact and solidification, Int. J. Heat Mass Transfer 45 (2002) 2229–2242.

[28] B.R. Bird, R.C. Armstrong, O. Hassager, Dynamics of Polymeric Liquids, Volume 1: Fluid Mechanics, second ed., John Wiley & Sons, Inc., 1987.

[29] D.T. Gawne, T. Zhang, Y. Bao, Heating effect of flame impingement on polymer coatings, in: C.C. Berndt, K.A. Khor, E.F. Lugscheider (Eds.), Proceedings of the ITSC 2001, ASM International®, Singapore, Materials Park, OH, 2001, pp. 307–313.